AIAA AVIATION Forum
June 15-19, 2020, VIRTUAL EVENT
AIAA AVIATION 2020 FORUM

10.2514/6.2020-3234

Atmospheric and Aero Disturbance Characterization for DE System Applications

Yakov Diskin*, Mitchell Grose, Matthew Whiteley†, Kevin Jackovitz, Richard Drye, Brandon Hampshire, Monte Owens, Eric Smith, Eric Magee
MZA Associates Corporation, Dayton, OH, 45430

Matthew Kalensky, Eric Jumper ‡, Stanislav Gordeyev
University of Notre Dame, Notre Dame, IN, USA, 46556

Aaron Archibald
Air Force Institute of Technology, 2950 Hobson Way, Wright-Patterson AFB, OH 45433

A system performance analysis from a series of Airborne Aero-Optics Laboratory - Beam Control (AAOL-BC) experiments is presented. Here, two laser beams are propagated between a moving aerial platform and a stationary ground receiver over an 8km slant path. Using the Path Resolved Optical Profiler System (PROPS) enables measurements of turbulence strength along the propagation path resulting in 30 range bins C_n^2 profiles. These profiling experiments ultimately allow key directed energy (DE) system propagation parameters such as Greenwood frequency, r_0, Rytov number, anisoplantic angle and Tyler frequency to be extracted. Additionally, the resulting open-loop jitter and open-loop Strehl are presented as well as how turbulence has a vastly different impact on air-to-ground DE systems versus ground-to-air DE systems. The profiles isolate the aero-optical contamination of the aircraft boundary layer within the range bins closest to the aircraft. This allows the aero-optical impact on DE systems to be quantified. The measurements and computed results are compared to the Hufnagel-Valley model (HV57) and high resolution atmospheric models from the Laser Environmental Effects Definition and Reference (LEEDR). This manuscript summarizes the data acquisition campaign, describes the technique used to isolate the aero-optical disturbance, and presents novel slant path analysis for DE system performance.

Nomenclature

A	=	value of C_n^2 strength at ground level
$C_n^2(h)$	=	refractive-index structure constant of turbulence, measures turbulence strength
d	=	subaperture separation
h	=	altitude above ground level
L	=	propagation path length
λ	=	wavelength
ω_s	=	slew rate
r_0	=	spherical-wave coherence diameter
s	=	transmitter source separation
θ_0	=	isoplanatic angle
V_g	=	ground wind speed
$V(h)$	=	Bufton wind model
w	=	root mean square windspeed
ξ	=	normalized path position
z	=	location along the propagation path
z_{iso}	=	location along the path of the isolated Difference of Differential Tilt Variance (DDTV)

*Research Scientist, Yakov.Diskin@mza.com
†Vice President and Senior Scientist, Matthew.Whiteley@mza.com
‡Aero-Optics Group Director, Roth-Gibson Professor, Department of Aerospace and Mechanical Engineering, EJumper@nd.edu

I. Introduction

UNDERSTANDING the effects and disturbances associated with the propagation of light through the atmosphere has been at the forefront of the Directed Energy (DE) and intelligence, surveillance, and reconnaissance (ISR) communities. The fluctuations in the refractive index, or optical turbulence, in the atmospheric medium affect the performance of optical systems. There are many system (aperture size, wavelength) and engagement (range, altitude, terrain) parameters that could influence a DE system's sensitivity to turbulence. Turbulence conditions fluctuate continuously with changes in weather, terrain, and altitude. Thus, for long propagation geometries, especially slant path geometries, the turbulence at one end of the path is often drastically different than the other.

Turbulence profilers compute path resolved measurements by utilizing multiple point sources (red and blue) on one end of the path and multiple observing sub-apertures in a wavefront sensor (WFS) on the other. Ray paths from two sub-apertures can cross and reveal information about a particular part of the propagation path. By analyzing different combinations of sub-aperture separations, the crossing of the red and blue beams can be moved to different parts of the propagation path. For widely separated sub-apertures and fixed sources, the crossing point is far from the receiving aperture. For minimally separated (side by side) sub-apertures, the crossing point is very close to the WFS. The MZA Path-Resolved Optical Profiling System (PROPS) turbulence sensor uses a cooperative source and wavefront sensor to measure the C_n^2 profile over a propagation path by calculating sub-aperture tilt variations. PROPS places a terminal at each end of the path and provides complementary path weighting functions with path isolation. The PROPS profiling technique uses both differential tilt variances and difference of differential tilt variances to achieve sensitivity along the entire path.

The Airborne Aero-Optics Laboratory - Beam Control (AAOL-BC) program conducted a series of experiments in which one PROPS terminal was placed in an aircraft and the other positioned on the ground. The aircraft continuously orbited the ground terminal, both transmitting red and blue laser beams to the ground station as well as receiving red and blue LED beams from the ground station. The experimental setup and data collection process is described in Section II. The turbulence measurements are compared to the standard and state-of-the-art turbulence models which are described in Section III. In Section IV, the measured profile isolates the aero-optical contamination from the aircraft boundary layer. In Section V, the DE system performance results are presented by using the measured profiles to address key system propagation parameters. The findings are summarized and concluded in Section VI.

II. Experimental Setup and Data Acquisition Campaign

The 2019 AAOL-BC profiling campaign [1] in Grand Rapids, Michigan, aimed at collecting air-to-ground path-resolved turbulence measurements for comparison and validation with 3D volumetric turbulence models. This was the third campaign of its kind with the first two occurring in 2018. These campaigns have yielded valuable data at relevant tactical geometries and ranges, the results of which are used to enhance system performance modeling capabilities for air-to-ground and ground-to-air DE systems.

In the campaign, MZA's PROPS was used to collect C_n^2 data between two terminals. The PROPS consists of two nearly identical terminals, each consisting of an optical receiver, color WFS, source assembly, and computer control. Unique source and sub-aperture geometries yield differential jitter measurements to compute path specific weighting functions resulting in a 30-bin profile. For this specific campaign, each terminal utilized 0.2032m receiving apertures and 1cm sub-aperture lenslet arrays. The ground station terminal was located at Coopersville High School in Coopersville, Michigan, and the other terminal was installed in an aircraft. During data collection, the aircraft continuously orbits around the ground station for approximately 3 hour flights with data collected on a per-orbit basis. The flight geometry is nominally a ground radius of 7.4km and an altitude 2.1km, yielding approximately an 8km slant path. Actual geometries during flight rely heavily on cloud altitude and wind conditions, thus exact geometries were recorded with a Trimble global positioning system (GPS) unit installed on the aircraft. Figure 1 is an image of the ground station's location with respect to Coopersville school facilities and nominal indications of orbit start and end on the morning of August 29th, 2019. The most fruitful flight occurred early in the morning so the orbit start and end locations were selected such that the ground station receiving aperture would not look in the direction of the sun.

Figure 2 shows images of the ground station PROPS terminal from the front and back. The terminal consists of a 0.2032m Meade telescope on a Meade LX200 gimbal mount. The sources, red and blue light emitting diode (LED)s (ground station used LEDs instead of lasers), are attached to the side, and the color WFS is on the back for data collection. Additional hardware components were added to the terminal for aircraft tracking. The added components included a Wide Field of View (WFOV) camera for aircraft acquisition, a Narrow Field of View (NFOV) camera

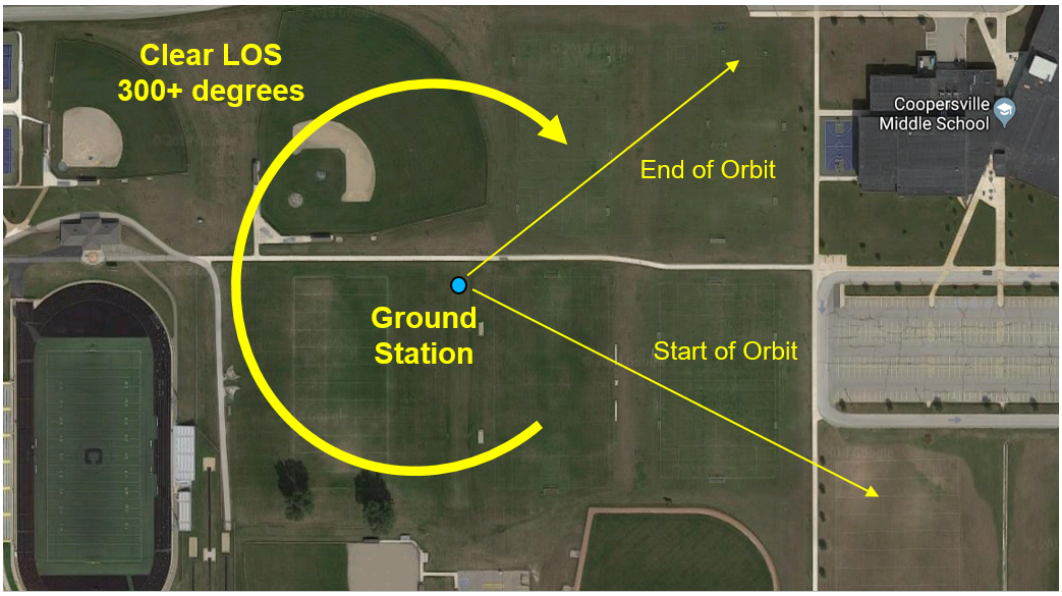

Fig. 1 Ground station setup location at Coopersville High School in Coopersville, Michigan. Aircraft continuously orbits the ground station in the clockwise direction for over 300°clear line-of-sight. To avoid looking into the sun, the ground station stopped aircraft tracking when looking east.

for aircraft fine-tracking, and a track beacon utilized by the air station for ease of tracking the ground station. A commercial-off-the-shelf (COTS) PROPS terminal utilizes the rails on the Meade telescope to maintain parallel optical axes between the telescope and LED source assembly. The customized PROPS terminal, depicted in Figure 2, shows additional mounting hardware designed to keep the LED source assembly in a vertical configuration. The LED sources are aligned to be parallel to the telescope optical axis. The vertical configuration was selected due to the anticipated potential horizontal clipping on the aircraft PROPS terminal. Setting the ground PROPS terminal's LED sources in a vertical configuration decreases the importance of preserving large horizontal sub-aperture separations on the aircraft PROPS terminal. Therefore, if horizontal clippings were to occur during the collection, the large sub-aperture separations would be preserved in the direction (vertical) of the source separation. Additionally, a COTS PROPS LED source assembly comes with an near infrared (NIR) track beacon. The customized ground station terminal included a modified beacon transmitting at 950nm. The new beacon would be detectable by the short-wave infrared (SWIR) track sensors on the aircraft.

The ground station procedure of tracking the aircraft and PROPS data was consistent throughout the campaign. Once the aircraft was spotted in the WFOV camera feed, the operator engaged the tracking algorithm onto the aircraft and applied tracking offsets until the aircraft appeared in the NFOV camera feed. Once in view, the user engaged track in the NFOV system. At the end of the orbit, tracking would be disengaged and PROPS data collection would end. Personnel then organized tracking and PROPS data by orbit and repeated the process. Collection software was set to collect 4000 frames at 200 frames-per-second (fps) every 30 seconds in order to achieve a high data yield.

Installing PROPS into the aircraft proved to be a significant challenge that ultimately led to refined installation procedures and guidelines for future aircraft implementation. Figure 3 shows three images: the assembly design, the successfully installed system in the aircraft, and in-flight user operation of the system. The receiving of light from the ground station propagated through the system as follows. Red and blue light from ground station LEDs would propagate through the atmosphere toward the aircraft, through a 0.3048m optical window, reflect off a 30cm mirror as part of the AOM360 AeroTech gimbal used for tracking, then propagate toward a 20.3cm Celestron telescope. At the base of the telescope aperture some light would be picked off by a mirror and reflected toward a FLIR camera attached to a Nikon Lens which acted as the WFOV camera for tracking. The remaining (majority) of light would be relayed through the telescope, exit out of the back, and encounter a 50/50 beam splitter. The splitter would propagate half of the received light into the color wavefront sensor, and the other half to the Allied Vision Technology (AVT) GoldEye CL-033 NFOV track camera. The video feeds from the WFOV and NFOV cameras were used by the tracking operator to engage tracking on the ground station, as shown in the bottom right of Figure 3. The GoldEye NFOV track camera

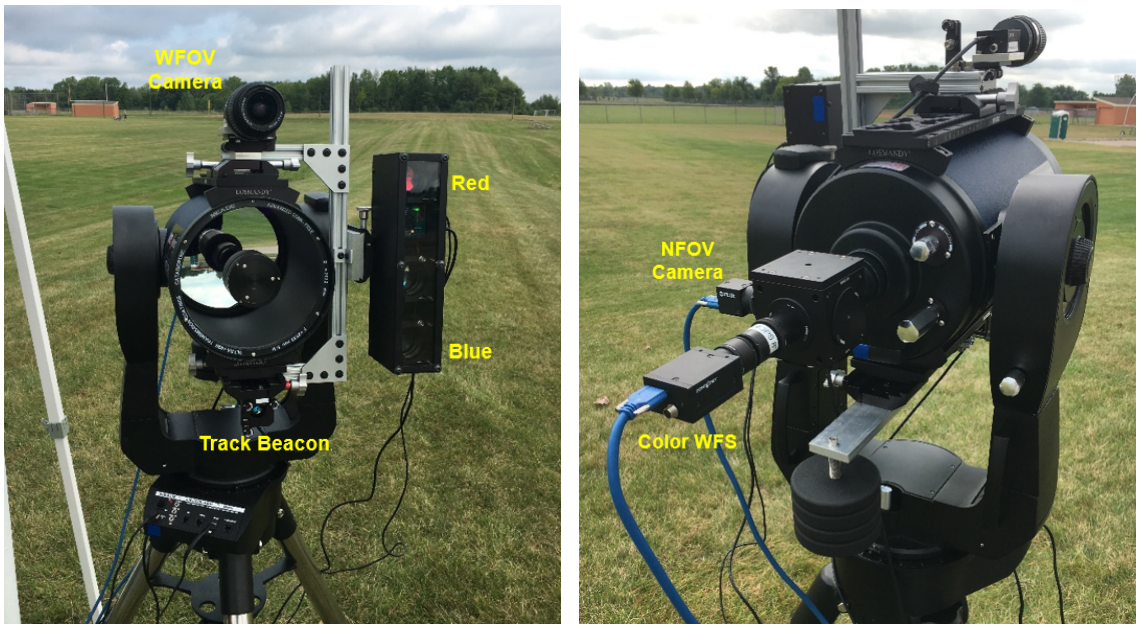

(a) Front of terminal showing the telescope, WFOV Camera, LED sources, and Track Beacon.

(b) Back of terminal showing the telescope, NFOV Camera, and Color WFS.

Fig. 2 Ground station customized PROPS terminal.

operates in the SWIR range, thus the modified track beacon on the ground station terminal in Figure 2 enabled beacon tracking for the aircraft station.

Tracking procedure in the aircraft was also consistent and repeated as follows. At the beginning of the orbit the tracking operator would manually rotate the AeroTech mirror to find the ground station in the WFOV camera feed. Simultaneously, the PROPS operator would begin data collection. Once the ground station was located in the WFOV, offsets would be applied to the tracking algorithm until the ground station appeared in the GoldEye NFOV Camera feed. At this point, tracking would be engaged in the NFOV until the end of the orbit. After the orbit, personnel would segment collected tracking and PROPS data into the folder corresponding to the orbit, and the process would repeat. Tracking the ground station from the aircraft was of notable difficulty due to the unpredictable mechanical jitter on the aircraft. Additional factors such as wind speed and winding heading at the aircraft altitude caused deviations from the bank angle. These deviations were corrected by the AeroTech gimbal, but were limited in the field-of-regard (FOR) due to the optical window. The top of Figure 3 shows the position relationship between the AeroTech gimbal and the optical window. Due to aircraft mounting constraints [1], the optical window was tilted 22.5° from vertical resulting in an elliptical FOR that is 28.2cm in the vertical direction and 30.5cm in the horizontal direction. The AeroTech gimbal was positioned so that the central rotation axis of the gimbal aligned with the center of the FOR provided by the optical window. The 30cm mirror on the AeroTech was angled at nominally 45° throughout the data collection. The angled mirror resulted in an ellipse that is 30cm (11.8") in the vertical direction and 21.1cm (8.4") in the horizontal direction. This produced a tight fit between the 20.3cm Celestron and 21.3cm horizontal span of the AeroTech mirror. As a result, the gimbal pointing could fluctuate horizontally ±1° without clipping. Corrections beyond the ±1° fluctuations would result in clipping of horizontal sub-apertures. These considerations drove the customized vertical orientation of the source assemblies on the ground and air terminals. Similar to the ground station, for high yield PROPS data acquisitions, the collection software was again set to collect 4000 frames at 200 fps every 30 seconds.

The propagation of light out of the aircraft to the ground station utilized laser source injection. As shown in the top of Figure 3, two lasers, red (637nm) and blue (405nm), were collimated to 5mm diameter out of 19mm lenses to a longpass dichroic mirror. The dichroic reflected the blue laser light and transmitted the red laser light toward a 200mm lens. After passing through the lens, the combined laser light was propagated 200mm into the back of the 20.3cm Celestron telescope (the same used for collection of ground station LED light). The combination of the 200mm lens and 2,000mm telescope yielded a 10X magnification. Thus the diameter of each beam was magnified to 50mm out of the telescope with 10 mrad divergence. Out of the telescope the beams were separated vertically by 12.7cm. After 8km of

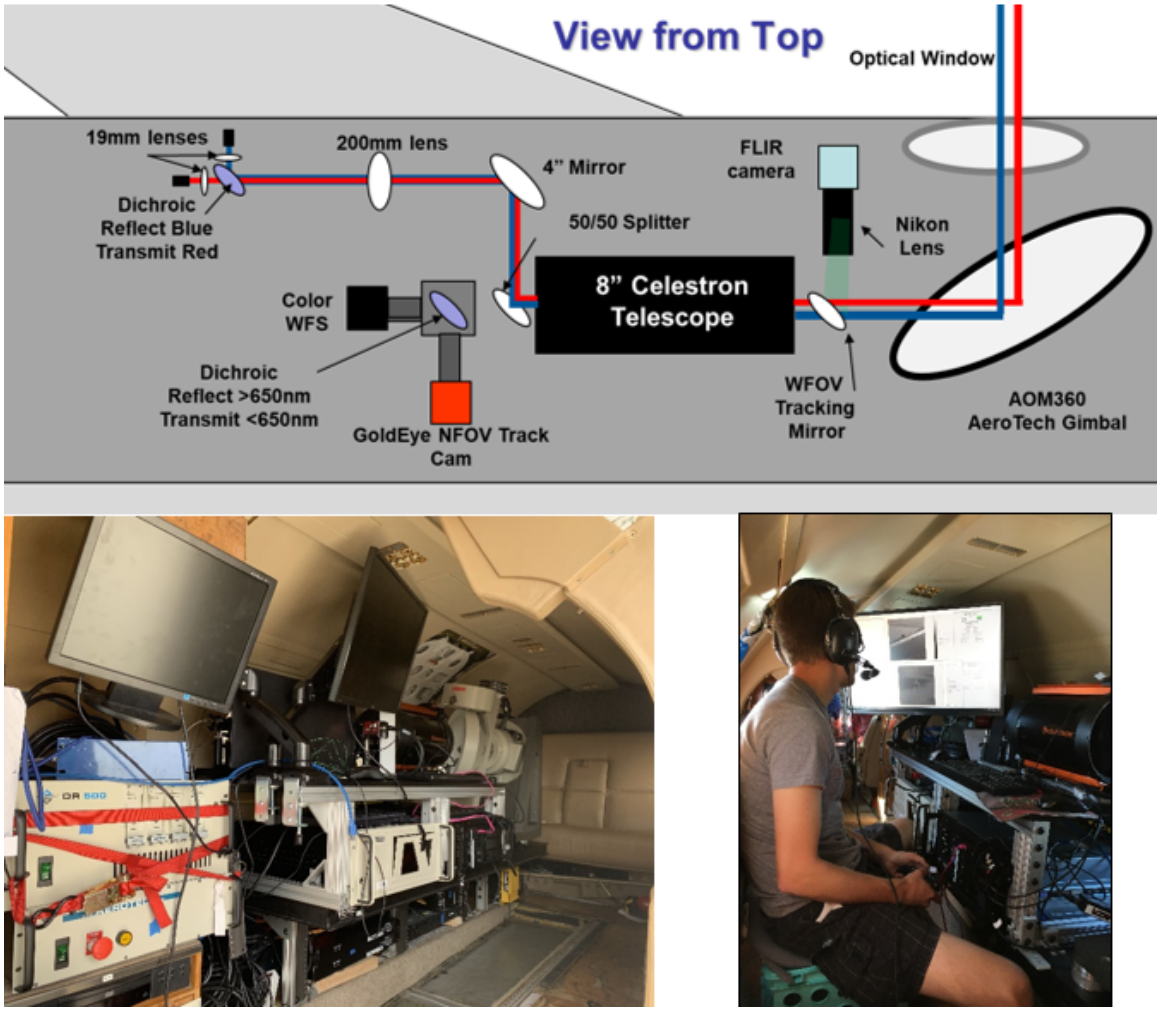

Fig. 3 Aircraft station LED source receiver, laser source emission, and tracking hardware successfully installed in the aircraft with in-flight user operation of the system.

propagation through the atmosphere, each beam was 160m in diameter. The maximum laser power was 125mW.

The advantage of using the laser source injection is to utilize one telescope for both reception and propagation of light. In 2018 campaigns, a bulky mechanical LED mount was installed in front of the telescope, leading to additional obscuration of the aircraft PROPS sub-apertures. Figure 4 shows the optical bench layout used in the 2019 campaign. For comparison, Figure 4 also shows the front of the telescope aperture in the 2018 design side-by-side with the 2019 design. Beneath each design image, Figure 4 also illustrates the accompanying WFS data. The WFS data shows approximately 110 sub-apertures visible in the 2018 design and approximately 170 sub-apertures in the 2019 design. The 2019 design yields over a 50% increase in the available WFS sub-apertures, which results in additional PROPS weighting functions described in Section IV. Both designs feature a vertical source assembly motivated by the tight fit between the gimballed mirror and optical window described above. In both designs, the aircraft sources are reflected off of the gimballed mirror. Therefore, the tracking and pointing from the aircraft system enables the sources on the aircraft to be visible (available) for the measurements made at the ground terminal. A robust tracking solution on the aircraft side is key to obtain measurements on both sides (aircraft and ground stations).

Although the 2019 design provided unobscured WFS data, there were some design flaws as well. In the 2018 design, the WFOV track camera pick-off mirror was positioned on the LED assembly between the red and blue source as shown in the middle of Figure 4. The pick-off mirror is aligned with the optical axis of the telescope, and therefore, aligned with the center of rotation of the gimbal. This design allows the WFOV track camera to utilize the full FOR provided by the gimbal and optical window. Unlike the 2018 design, the 2019 design was motivated by removing additional

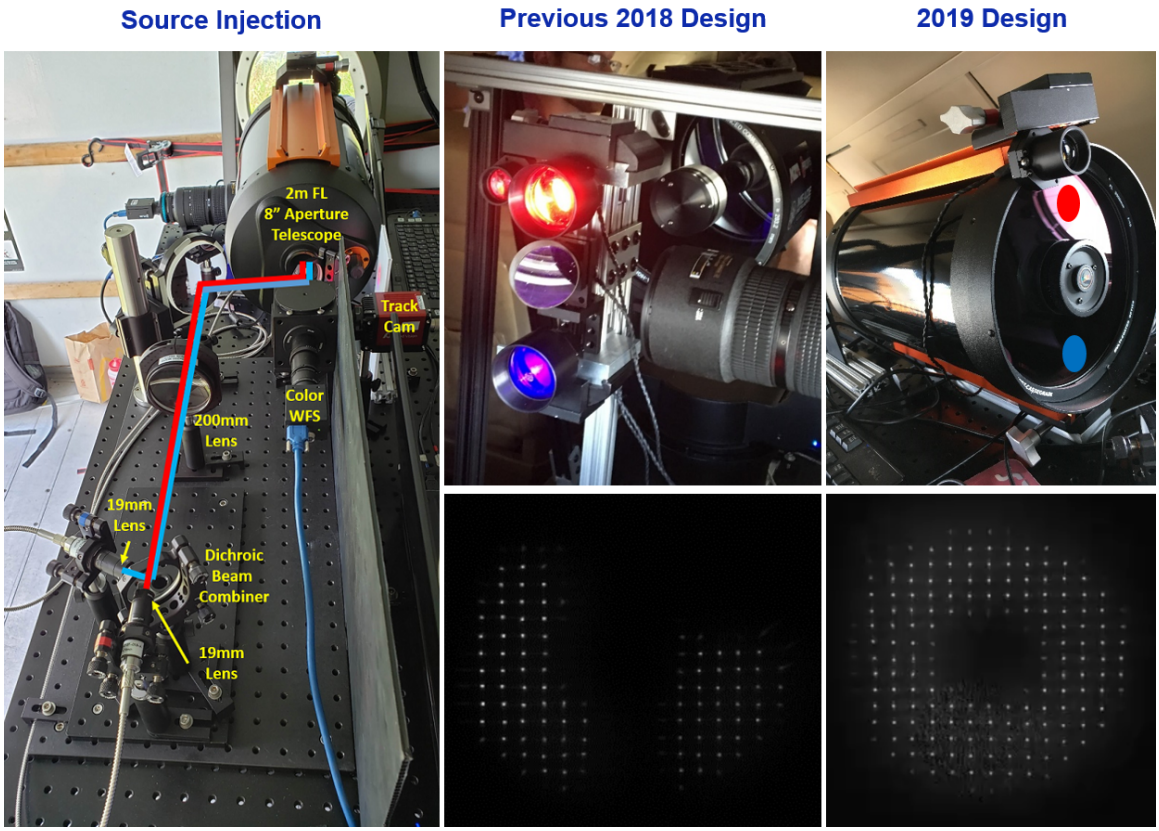

Fig. 4 Aircraft laser source injection design; 2018 campaign mechanical LED mount with obscured sub-apertures; 2019 campaign laser source injection with unobscured sub-apertures.

obscurations in front of the telescope aperture, and moved the WFOV track camera and pick-off mirror beneath the 0.2032m Celestron telescope. As a result, in the 2019 design, the WFOV track camera was no longer on the optical axis and no longer aligned with the center of rotation of the elevation axis of the AeroTech gimbal. Under nominal conditions, the WFOV track camera used the pick-off mirror to image the reflection of the lower portion of the gimballed mirror. Since the WFOV track camera was attached to a Nikon lens with a 0.0508m aperture, it only required a small portion of the gimballed mirror in order to successfully record imagery and perform tracking. Unfortunately, the FOR for the WFOV track camera was significantly smaller in the 2019 design. In the presence of high winds or turbulent flight conditions, the aircraft would deviate from nominal bank angle and the system would rely on the gimbal to compensate for the aircraft motion. During these non-nominal realistic conditions, the WFOV track camera would be clipped by the edges of the optical window. As a result for the WFOV track camera clipping, the aircraft PROPS terminal was able to record about 60% of each orbit.

III. Atmospheric Models

The turbulence measurement campaigns can be used to verify and validate turbulence modeling. The analysis compares the measurements to the most commonly used altitude-dependent turbulence model, the Hufnagel-Valley 5/7 (HV57) model, as well as the Air Force Institute of Technology (AFIT) led Laser Environmental Effects Definition and Reference (LEEDR) volumetric turbulence model [2].

A. HV57 Model

The Hufnagel-Valley model was developed to characterize optical turbulence, C_n^2, as a function of altitude above ground level (AGL) [3]. It has become a standard atmospheric model that is commonly used in system performance

simulations. The Hufnagel-Valley model is described as

$$C_n^2(h) = 0.00594(\frac{w}{27})^2(10^{-5}h)^{10}e^{-h/1000} + 2.7\times10^{-16}e^{-h/1500} + Ae^{-h/100}, \tag{1}$$

where h is altitude AGL in meters [m], w is the root-mean-squared (RMS) windspeed in meters per second [m/s] and A is the value of C_n^2 strength at ground level in $m^{-2/3}$ [4]. The RMS wind speed in Equation 1 is determined from

$$w = \left[\frac{1}{15\times10^3}\int_{5\times10^3}^{20\times10^3} V^2(h)dh\right]^{1/2}, \tag{2}$$

where $V(h)$ is described by the Bufton wind model [5, 6] written as

$$V(h) = \omega_s h + V_g + 30e^{-\left(\frac{h-9400}{4800}\right)^2}. \tag{3}$$

V_g is the ground wind speed and ω_s is the slew rate associated with a satellite moving with respect to an observer on the ground.

The Hufnagel-Valley profile is popular for theoretical studies because it allows for variations in high-altitude wind speed and ground level C_n^2. A particular iteration of the model uses $w = 21m/s$ and $A = 1.7\times10^{-14}m^{-2/3}$ to yield 5 cm for atmospheric coherence diameter, r_0, and 7 μrad for isoplanatic angle, θ_0, at wavelength λ = 0.5 μm. This is the HV57 model and its C_n^2 strength as a function of altitude AGL is illustrated in Figure 5. The curve shows C_n^2 at ground level to be 1.7×10^{-14} and rapidly decreasing with increasing altitude. At an altitude of 1km AGL, the C_n^2 has decreased by two orders of magnitude to approximately 2×10^{-16}. Interestingly, the HV57 model shows a turbulence increase above an altitude of 6km AGL.

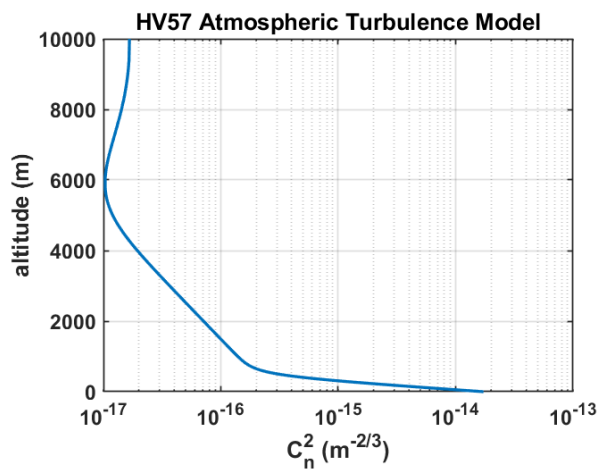

Fig. 5 HV57 atmospheric turbulence C_n^2 model as a function of altitude AGL.

B. LEEDR Model

The measurements made in this study will be compared with the state-of-the-art LEEDR weather cube models [7]. The most current released version of the LEEDR software makes use of $\frac{1}{2}$ degree and $\frac{1}{4}$ degree resolution Global Forecast System (GFS) data. Within the continental United States (CONUS) the $\frac{1}{2}$ degree resolution creates an approximately 50km grid while the $\frac{1}{4}$ degree resolution creates an approximately 25km. GFS models [8] are operated by National Oceanic and Atmospheric Administration (NOAA) and run 4 times per day with forecasts every 3 hours out to 10 days, then every 12 hours out to 16 days. Re-analysis data is readily available and archived back to 2007.

MZA and AFIT have worked to update the LEEDR weather cube model to work with National Centers for Environmental Prediction (NCEP) generated High-Resolution Window (HIRESW) Forecast System. The HIRESW data comes from regional Weather Research and Forecasting (WRF) models. HIRESW is only available for the United States, Guam, and Puerto Rico. The HIRESW data provides a 5km uniform grid (Lambert projection). HIRESW is run 2 times per day with forecasts every hour out to 48 hours. Figure 6 illustrates how the increase in spatial resolution affects the three dimensional (3D) LEEDR weather cubes. Each vertical line represents a latitude/longitude grid point in the weather cube and spans 0 to 10km altitude AGL. In this example, the depicted optical parameter is the total extinction coefficient. The key advantage of using the HIRESW forecasts over the GFS forecasts is the increased spatial (5km) and temporal (hourly) resolution.

The script for generating LEEDR weather cubes includes updated surface level C_n^2 and altitude scaling turbulence models. The updated models leverage machine learning [9, 10] to learn weather-induced surface level turbulence and altitude scaling trends. Figure 7 (left) shows how the LEEDR weather cubes integrate the multiple turbulence and altitude scaling models. LEEDR uses the surface level altitude scaling up to 100m AGL, then linear interpolation

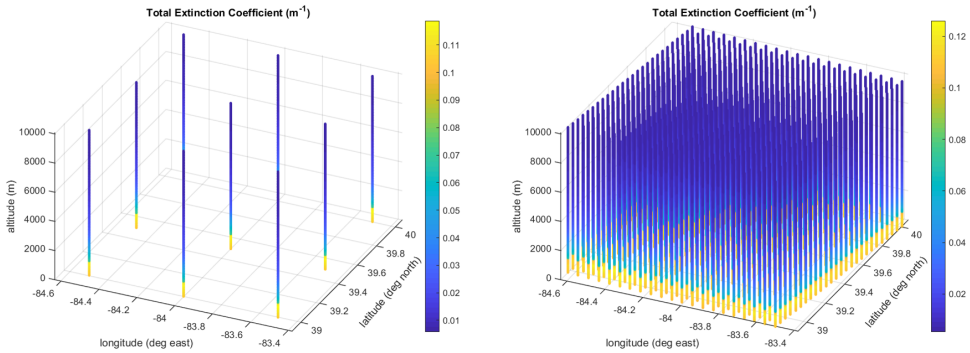

Fig. 6 Spatial resolution of the LEEDR weather cube using GFS $\frac{1}{2}$ degree (left) and WRF HIRESW (right). Each vertical line represents a latitude/longitude grid point in the weather cube.

between the scaled value at 100m AGL and LEEDR computed value at 200m AGL. Above 200m AGL, the turbulence profile is computed from LEEDR.

To compare our PROPS measurements with LEEDR weather cube models, these models had to be generated for the 3D volume that encompasses the propagation geometries in the Grand Rapids, Michigan area. The models are generated using forecast hours available for the times of the PROPS data collection. The cubes are generated using HIRESW data at 5km resolution. Figure 7 (right) shows terrain altitude mean sea level (MSL) using the digital terrain elevation data (DTED) over the spatial extent of the weather cubes. The weather cubes encompass a much larger region than the PROPS propagation geometry. Terrain data is used to appropriately calculate the altitude AGL for various propagation geometries. Relevant locations are labeled: (1) Coopersville, MI, where the ground station was set up, (2) downtown Grand Rapids, MI, and (3) Northern Jet Management (NJM) at Gerald R. Ford International Airport (GRR), the home base of the aircraft used in these experiments. For the cubes represented in 7 (right), the x-axis (longitudes) is 70 km and the y-axis (latitudes) is 90 km. Additionally, the 8km orbit that the aircraft flew around Coopersville is shown. It is interesting to note that the orbit passes over varying terrain features such as hills and river valleys. The change in terrain elevation beneath the orbit is expected to cause variations in the turbulence measurements.

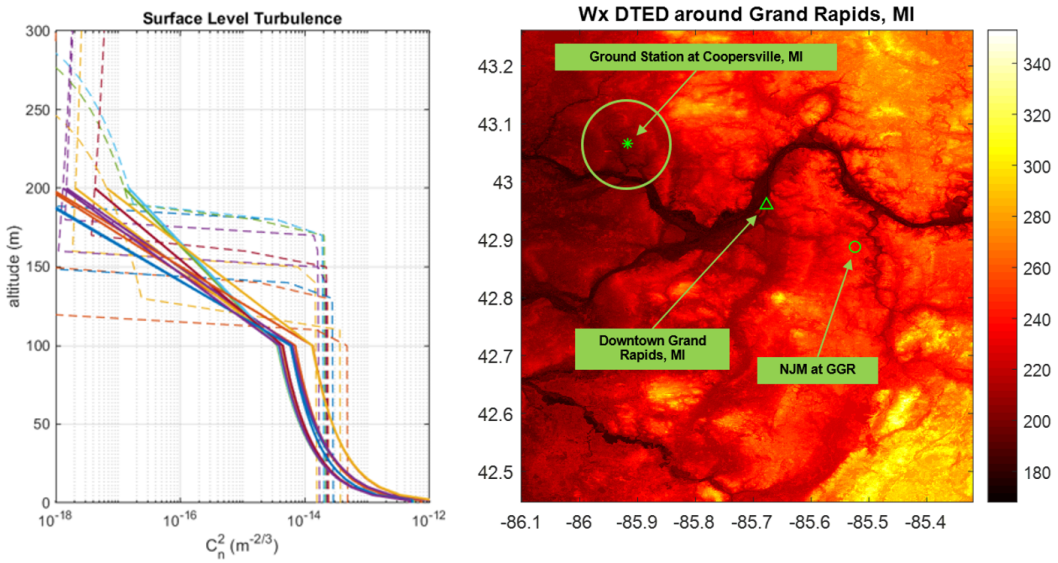

Fig. 7 (Left) Dashed lines are LEEDR values. Solid lines are the MZA surface model. Each line is a different profile (latitude/longitude) with a LEEDR weather cube. (Right) DTED from HIRESW weather cube generated over Grand Rapids, Michigan, during the experiment.

IV. Atmospheric and Aero-Optical Disturbance Measurements

The PROPS measurements provided the C_n^2 values along the optical propagation path. The profiles allow for isolating the aero-optical disturbance within the profile bins closest to the aircraft.

A. Path-Resolved Turbulence Profiling

The PROPS makes use of the well-established Difference of Differential-Tilt Variance (DDTV) method which has been the basis for prior turbulence profiling research [11, 12]. The PROPS computes differential-tilt variance (DTV) by measuring wavefront slopes from two spatially-separated LED sources. The DTVs are computed from so-called "separate path" geometries where the paths from the sources to receiver aperture do not intersect, and from "crossed path" geometries where the paths from the sources cross-over along the propagation path. These path geometries are illustrated in Figure 8 (left).

The weighting functions computed from these path geometries are shown in Figure 8 (middle). In the case of the separate-path DTVs, the resultant path-weighting function has contributions over the full path, similar to the weighting function for a differential image motion monitoring (DIMM) system. When the source separation is zero, $s = 0$ in Figure 8 (left), the propagation paths converge to a common source. This path weighting function is proportional to $(1 - z/L)^{5/3}$, familiar as the path weighting when computing the spherical-wave coherence diameter, r_0 as:

$$r_0 = \left[\frac{2.91}{6.88} \left(\frac{2\pi}{\lambda} \right)^2 \int_0^L C_n^2(z)(1 - z/L)^{5/3} dz \right]^{-3/5}, \tag{4}$$

where L is the total path length, z is the location in the path, and λ is the wavelength used for calculation, 550nm. Indeed, those geometries are identical to the source-receiver geometry of a traditional DIMM sensor. When examining the crossed-path geometries for the PROPS, the DTV includes a sharp reduction where the propagation paths of each source intersect, illustrated in Figure 8 (middle). The DDTV is computed by subtracting the crossed-path DTV from the separate-path DTV, yielding a turbulence measurement whose weighting function is isolated in the path. This DDTV calculation and resultant path-specific weighting function is presented in Figure 8 (right). Another beneficial aspect of such DDTV measurements is a natural noise-suppressing character in the data processing when the noise is uncorrelated and at similar levels as the underlying differential-tilt variances [11, 12].

The location of the resultant path-specific weighting function from the DDTV measurement with crossed-path geometries is a function of the separation of the sub-apertures. The maximum separation is limited by the receiving

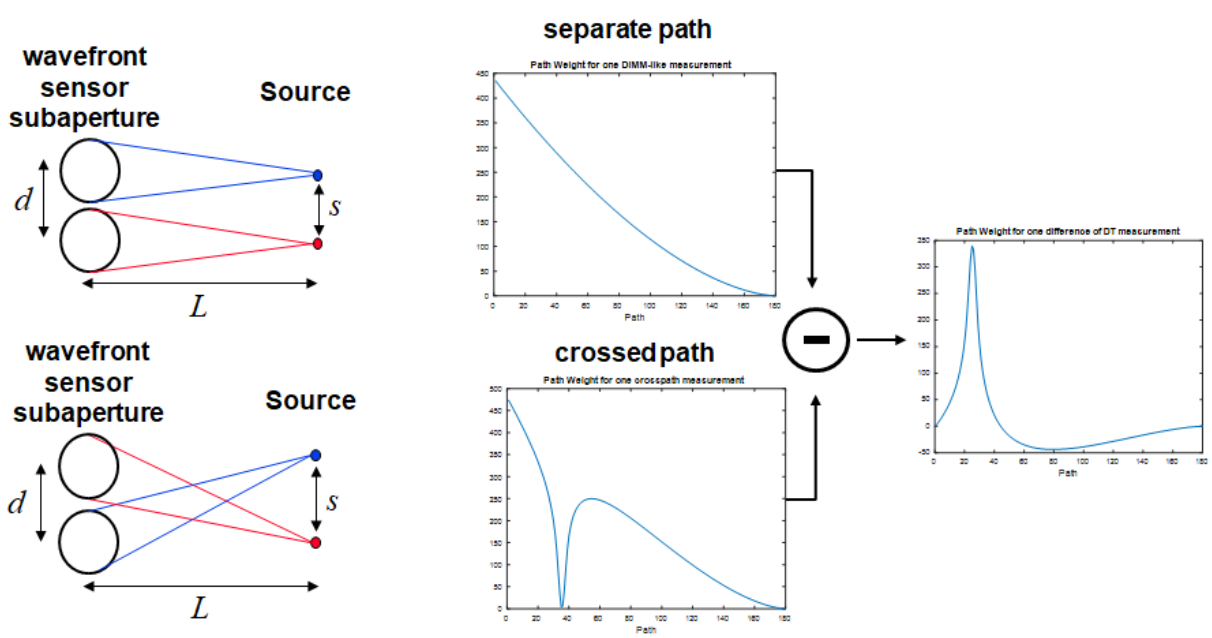

Fig. 8 DTV geometries for PROPS.

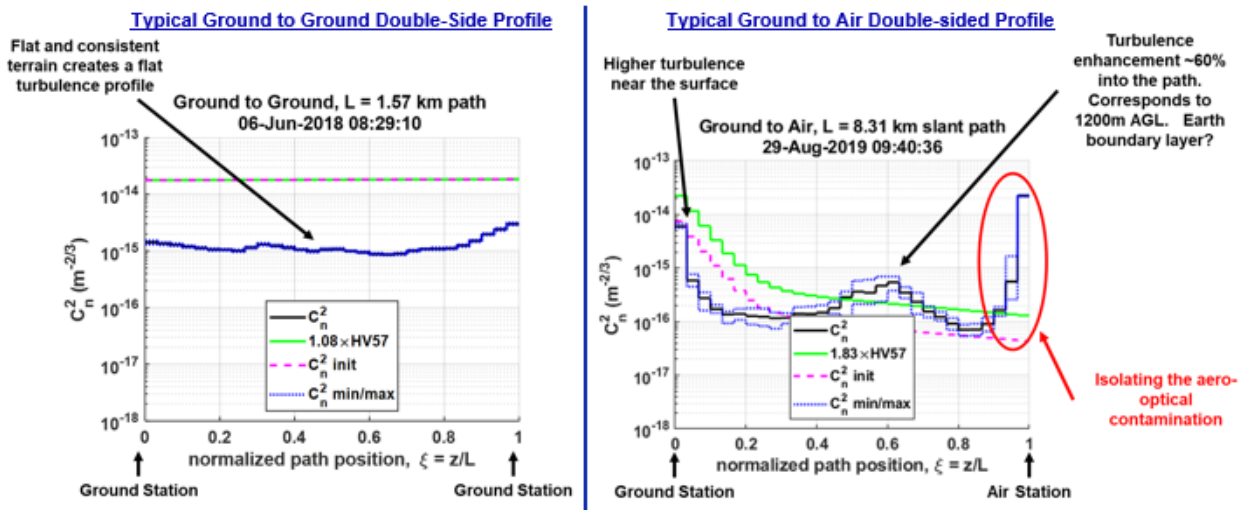

Fig. 9 Comparison between a typical ground-to-ground (G2G) PROPS profile versus a ground-to-air (G2A) PROPS profile.

telescope aperture and sub-aperture sampling. The location along the path of the isolated DDTV, z_{iso}, is given by

$$z_{iso} = \left(\frac{d}{d+s}\right) L, \tag{5}$$

where d is the sub-aperture separation, s is the source separation, and L is the path length. For example, when $d = s$, then $z_{iso} = L/2$. When d is decreased, the isolation region moves toward the receiver. When d is increased, the isolation region moves toward the sources. By exploiting the full range of sub-aperture separations supported by the WFS geometry in the receiver telescope, the greatest diversity of turbulence measurements is obtained. To complete the profiling operation, PROPS utilizes the full extent of sub-aperture separations to obtain multiple path-specific weighting functions in addition to the broad weighting functions formed from the separate-path measurements. When using bidirectional terminal measurements, the DDTVs from both terminals are employed in the profiling operation for high-confidence full-path profiling.

The standard PROPS output shows 30-bin path resolved turbulence strength C_n^2 along a normalized path. Figure 9 compares a typical PROPS ground profile to a typical PROPS slant path profile. A typical ground-to-ground PROPS profile captures terrain induced turbulence effects. If there are no significant variations in path altitude above the terrain, or other environmental features, the profiles tend to be flat. A typical ground-to-air PROPS profile primarily captures the altitude related turbulence effects. There is strong turbulence near the ground that quickly drops as the measurements rise in altitude. Interestingly, the PROPS measurements also capture a turbulence enhancement approximately 60% into the path (an altitude of 1,200m AGL) that could be attributed to the Earth Boundary Layer. Also, the profile bins nearest to the aircraft contain significant disturbances that can be attributed to the aero-optical contamination. The contamination is isolated in the first 2-3 bins nearest to the aircraft. A key advantage of the DDTV is it allows analysts to isolate non-atmospheric optical disturbances, which in this case is the aero-optical contamination.

B. Removing Aero-Optical Contamination

An illustration of the removal of aero-optical contamination is shown in Figure 10. The two plots each show the PROPS measured C_n^2 profiles as a function of altitude from a single orbit. The example depicted an arbitrary orbit, orbit 14, on August 29th, 2019 around 9:30AM. Within the plots the x-axes are logarithmic-scale C_n^2 and the y-axes are linear-scale altitude AGL. Plot (a) contains the raw profiles and the HV57 profile (green) modeled from the path geometry during orbit 14. Each raw PROPS profile is labeled with a timestamp representing when the time the WFS data was collected. Since HV57 is only altitude dependent, there is a single model profile for orbit 14. Apparent in (a) is the consistency in profiles near ground-level and bumps in C_n^2 from 900m to 1400m altitude AGL. Turbulence dips in magnitude around 1500m for nearly all the measured profiles in orbit 14. After the dip is another bump in turbulence at from 1800m to 2000m altitude AGL. These high-altitude bumps are a result of aero-optical contamination from the

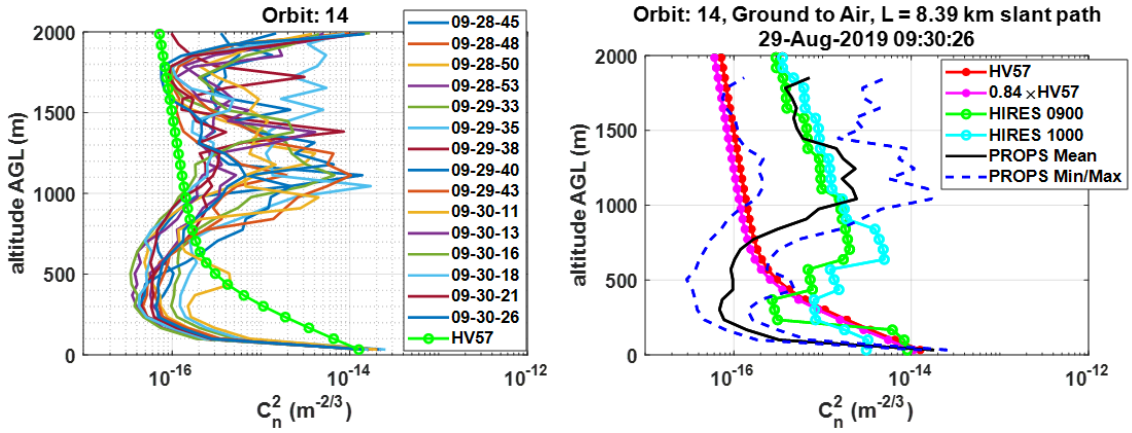

(a) Measurements within one orbit **(b) Measurements statistic for one orbit.**

Fig. 10 Eliminating the PROPS profile bins closest to the aircraft reduced the aero-optical contamination of the atmospheric profile measurements and enables a direct comparison to C_n^2 modeling.

plane and are subject for removal. Figure 10 (b) is a statistical summary illustration of the results from orbit 14. Plot (b) illustrates the same measured PROPS profiles from (a), but plotted as a mean in solid black and min/max as dotted blue lines. As shown by the lack of measured data above 1800m altitude AGL, the aero-optical disturbance near the aircraft is eliminated. By removing the aero-optical contamination bins, the measurements and model atmospheric profiles are more directly comparable. Also illustrated in (b) are LEEDR weather cube profiles computed for times surrounding the orbit, 09:00 in green and 10:00 in cyan. Since the LEEDR profiles are path dependent, there are multiple curves per cube, each representing the geometries of the measured profiles. Figure 10 (b) is illustrating the mean value for each altitude bin of HIRESW forecast. For reference, in earlier tests, the green line represents the HV57 model for the plane's geometry during orbit 14, which is only altitude dependent. At surface level, (b) shows that the LEEDR weather cubes and measured C_n^2 have similar magnitudes. Additionally, the bumps in turbulence from 900m to 1400m captured by the PROPS profiles are also apparent in the weather cubes. Generally, the measured profiles have similar shape to the weather cubes. Magenta and red are the HV57 model profiles calculated with and without an α multiplier, respectively. The α multiplier is derived from the average of the measured coherence diameter, $r_{0,measured}$, for each profile and calculated HV57 coherence diameter, $r_{0,HV57}$, for the path geometry. It scales the HV57 model profile so its r_0 matches the measured r_0. Specifically, α is calculated by

$$\alpha = \left(\frac{r_{0,measured}}{r_{0,HV57}} \right)^{-5/3}. \tag{6}$$

Figure 10 (b) shows that the average contamination-removed PROPS profiles in orbit 14 roughly agree in shape with the LEEDR weather profiles from surface level to 1000m altitude AGL. Beyond 1000m the average measured profiles match well with the LEEDR weather cubes.

The PROPS profiles are typically analyzed on a normalized path position plot. Figure 11 illustrates another perspective of the results from removing aero-optical contamination from the atmospheric profiles. Plots (a) - (d) are logarithmic axis C_n^2 as a function of normalized path position. On the x-axis, the zero-position is the air terminal and the one-position is the ground terminal. Plots (a) and (b) show a single PROPS profile without and with aero-optical contamination. The profile is represented by both red and black lines. The red line illustrates how much normalized path position each bin represents, whereas the black line simply connects the center of each bin. Also shown in green is the reference HV57 model. (a) and (b) show how the PROPS measurements compare with HV57. Turbulence strength at the ground terminal, x-axis equals 1, is similar, but measurements indicate turbulence falls off with slant-path range significantly faster than modeled. Additionally, the PROPS measured a bump in turbulence about 40% into the path from the air-perspective that is not captured by the model. With aero-optical contamination removed, plot (b), the turbulence characteristics near the air station are more consistent with expectation and model, indicating the importance of isolating those bins. Plots (c) and (d) in Figure 11 contain all orbit 14 PROPS measurements without and with aero-optical contamination, and reference HV57 in green. These results show the same trend as in (a) and (b). At the

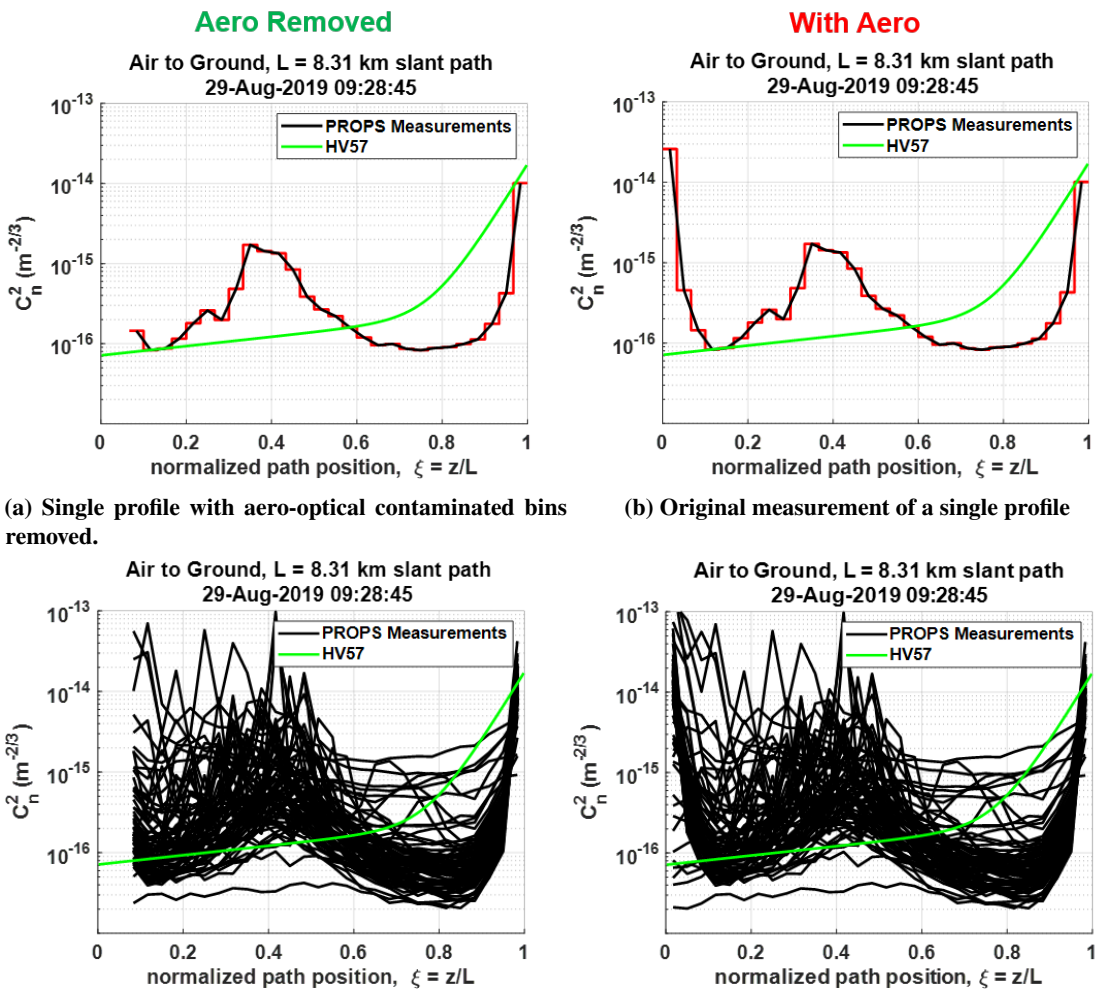

(a) Single profile with aero-optical contaminated bins removed.

(b) Original measurement of a single profile

(c) All measurements aero-optical contaminated bins removed.

(d) Original measurements with aero

Fig. 11 The aero-optical contaminate can appear as high C_n^2 values in the profile bins closest to the aircraft.

ground terminal model and measurements are in good agreement, but measurements indicate turbulence falls off faster than modeled. The characteristic bump 40% into the path from air perspective is still evident. The spike in turbulence close to the air terminal is consistent in all profiles, increasing confidence it's not atmospheric induced.

A unique aspect of this data collection is the continuously changing geometry of the PROPS measurements. Figure 12 shows the measurement summary of an arbitrary orbit, orbit 16, double-ended profiles with geometry perspective. The background is a satellite map where the center is the location of the ground station. The plane's slant range is illustrated by the blue-purple circle, where blue indicates a shorter slant path and purple a longer slant path. Reference the colorbar at the left of the Figure. The difference in slant path range is a function of wind speed and direction that impacts the aircraft's orbit. The wind from the Southwest elongates the orbit in the Northeast direction. The measured double-ended profiles are illustrated by the spokes extending from the map center to the slant range circle. The magnitude of C_n^2 at each bin profiled by PROPS is represented by the color of that bin. Red indicates high C_n^2 of 10^{-13}, and blue indicates low C_n^2 of 10^{-17}, as referenced by the colorbar at the right of Figure 12. Many single-ended profiles were generated from orbit 16, but only double-ended profiles are shown. The single sided profile measurements require time-synchronization between ground and air stations. For example, as mentioned in Section II, the ground terminal and aircraft terminal collection 4000 frame sequences at 200 fps. The 20 second recording would occur approximately once per minute. Therefore, if the ground station and air station fall out of synchronization then the orbit results in many single sided profile measurements but few double sided measurements. This synchronization challenge results in

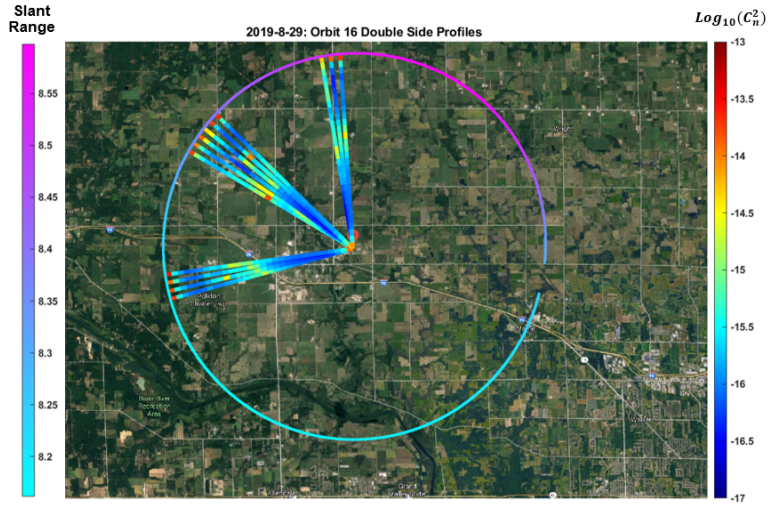

Fig. 12 Single orbit measurements. Double-ended time synchronization results in several PROPS profiles per orbit.

large gaps between groups of double-ended profiles. Like shown in previous Figures, the aero-optical contamination is illustrated by the yellow and red bins near the slant-path circle in Figure 12. The characteristic bump in C_n^2 around 40% into the propagation path from air (plane) to ground is also illustrated by the green-yellow bins surrounded by dark blue bins.

V. DE System Performance

The results of the analysis focus on comparing double-ended PROPS measurements with HV57 and LEEDR weather cube models. Additionally, this section shows the DE system performance analysis for an aircraft system looking down and for a ground system looking upward. The comparison of air-to-ground (A2G) engagements versus ground-to-air (G2A) engagements will use an arbitrary but realistic DE system with a 30cm aperture operating a 1MW, 1μm laser.

A. Measurements vs Modeling

The measurements versus modeling analysis is summarized by comparing the spatial representation of an ensemble of measurements to the turbulence models generated for that time. Figures 13a, 13b, and 13c show the HV57 profile, a LEEDR weather cube profile, and measured PROPS profiles, respectively, on a spatial map of the experiment site similar to Figure 12. Like before, the C_n^2 strength is represented by the color of each bin. Dark red is strongest and dark blue is weakest, as referenced by the colorbar at the right of each Figure. Since HV57 is only dependent on altitude, the profiles around the orbit are identical as seen in Figure 13a. The 10:00 LEEDR weather cube generated from HIRESW numerical weather prediction (NWP) data in Figure 13b is dependent on terrain so there are slight variations in each spoke, but over relatively short distances the differences are minimal. There is a strong contrast between Figures 13a and 13b. HV57 models turbulence that is much stronger at the ground station (center of the spokes) and falls off quickly with altitude, but LEEDR models turbulence at medium strength (approximately 10^{-15}) over the entire propagation path with an enhancement about 30% into the path from ground terminal to air terminal. Figure 13c contains all double-ended PROPS measurements over the course of one hour of flight. The aero-optical contamination is apparent as the orange-red bins at the edge of the spokes. Like HV57, but unlike LEEDR, measurements indicate strong turbulence at the ground terminal (center of spokes). Measurements show that turbulence near the surface decreases rapidly with increasing altitude. Then, turbulence starts to increase again several hundred meters above the ground, which is possibly due to the Earth boundary layer. The LEEDR model in 13b captures a turbulence enhancement in the path as well, indicated by the orange ring. Overall, the spatial comparison of PROPS measurements reveals interesting similarities and differences in the characteristics between measurements and modeling. These measurements will be used to further enhance the modeling capabilities.

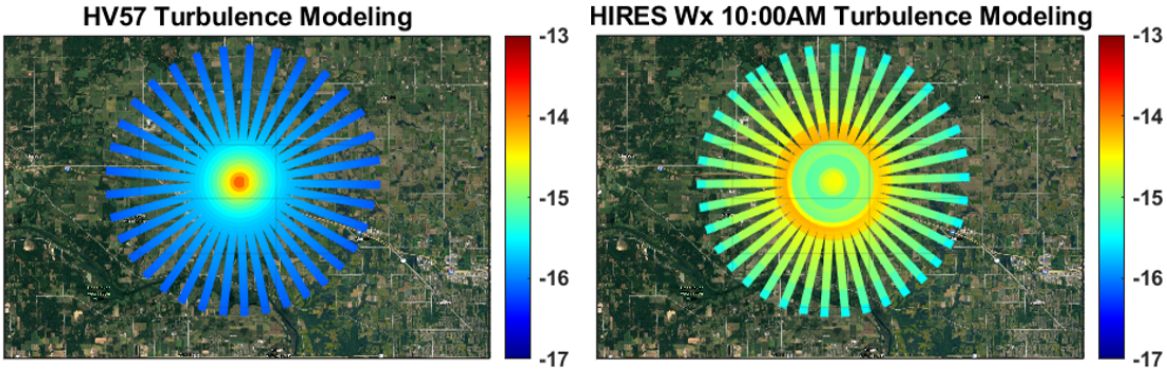

(a) HV57 model on spatial map.

(b) HIRES 10:00 LEEDR WxCube on spatial map.

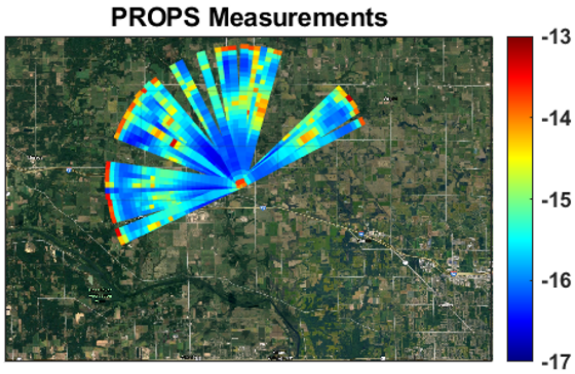

(c) PROPS measurements on spatial map.

Fig. 13 Compare modeling and measurements on a spatial map of the experiment site.

Another interesting aspect captured by the measurements is the altitude scaling relationship between C_n^2 and altitude AGL. Figure 14 shows C_n^2 (on a logarithmic scale) as a function of logarithmic scale and linear scale altitude in 14a and 14b, respectively. Each plot covers multiple measurements and contains the same data: double-ended PROPS measurements, 09:00 and 10:00 LEEDR weather cube profiles for each measurement geometry, and the HV57 profile. The green curve in each plot is the 50%-tile PROPS profile, essentially the median profile. The results are plotted with altitude on a logarithmic scale in 14a because a linear relationship in this loglog plot indicates a power law relationship. It is clear that both measurements (black curves) and LEEDR profiles (blue and cyan curves) have a power law relationship to approximately 100m altitude. This characteristic is implemented into LEEDR, but measurements confirm power law is occurring. Note the measurements (black curves) begin at 30m altitude AGL since each data point is the PROPS bin center. Since each PROPS bin is approximately 60m in altitude, the bin center of the first bin is 30m altitude AGL. Beyond 100m, the measurements are linear with smaller slopes until about 200m AGL, indicating a weaker power law. The LEEDR models, however, shift away from power law and indicate an increase in turbulence. At no point in the profile does the HV57 model (red dashed line) show power law. Generally, the curves on linear altitude scale look smoother than on logarithmic scale as a result of the characteristic of logarithms, but with altitude on linear scale, the power-law characteristics of the measurements and models are difficult to distinguish. While the logarithmic scale shows that there is a power law at lower altitude AGL, the linear scale shows that there is agreement at higher altitude AGL. Above 1000m AGL, the measurements and LEEDR follow a similar trending slope. In conclusion, the measurements reveal two key observations. First, a power law exists at lower altitudes near the surface and the power law used in the modeling is not quite the same. Second, the LEEDR model has the right general trend although some of the turbulence to altitude slopes are still different. These observations cast an encouraging verification of the modeling performance and highlight potential area where the modeling could be improved.

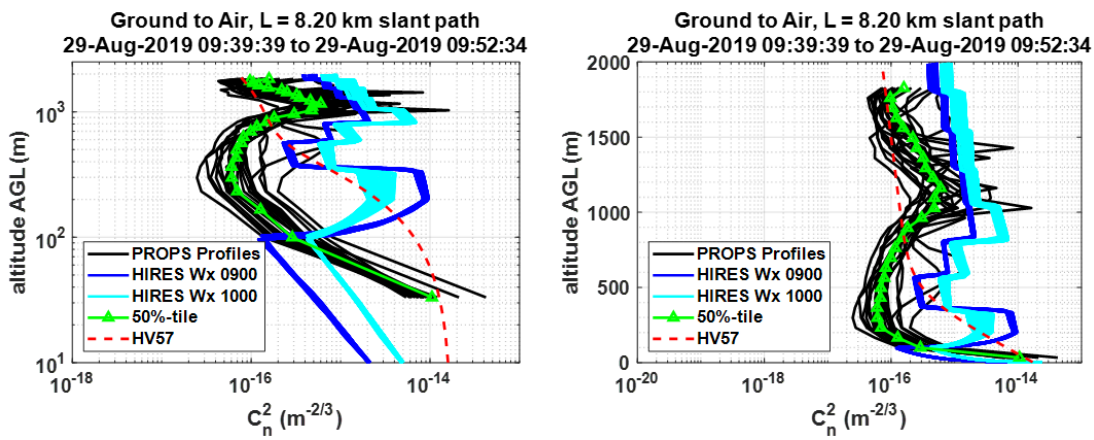

(a) Altitude logarithmic scale. **(b) Altitude linear scale.**

Fig. 14 Compare modeling and measurements with logarithmic and linear altitude scales.

B. System Performance Modeling With and Without the Aero-Optics

The atmospheric conditions impact the performance capability of any DE system. For A2G system, the aero-optical effects around a DE system look out of an aircraft and are optical distortions imposed on a propagating laser beam due to a varying density field around an aircraft, as the density field affects the local index-of-refraction[13–16]. The density variations are caused by either compressibility effects at flight Mach numbers above 0.2 or by pressure variations. The physical cause of aero-optical effects is different from atmospheric optical effects, which are caused by total temperature variations in the atmosphere.

This section presents system performance modeling as a function of the measured C_n^2 profile. The analysis focuses on capturing differences in performance with and without the inclusion of aero-optical contamination. Removal of the two bins closest to the air terminal allows for better understanding of atmospheric characteristics on system performance. Leaving the aero-optical contamination in the data set allows the error associated with these disturbances to be assessed. First, measured and modeled system quantities are presented with and without contamination. Then, using these measurements and modeled quantities (with HV57 & LEEDR), the system performance (including open loop jitter and open loop Strehl) is estimated.

Figure 15 compares four system parameters – spherical Rytov number, Isoplanatic Angle, Greenwood Frequency, and Tyler Frequency – between results with and without aero-optical contamination. Each plot contains PROPS measurements, LEEDR weather cube (in blue), and HV57 model (in green). The hourly temporal resolution of LEEDR results in lulls in this model's results. First, comparing spherical Rytov number in Figure 15 (a) and (b), generally the removal of aero-optical contamination does not yield significant differences. The clustering of measurements between each plot are similar, and magnitude differences are minimal. Rytov is most sensitive to the turbulence conditions at the middle of the path. The mid-path conditions do not change between (a) and (b), the only differences in the turbulence profile are in the bins closest to the aircraft where Rytov has minimal sensitivity. Rytov measurements have more agreement with the HV57 model than the LEEDR model, shown by most of the measurements to be around the green line. In (c) and (d), isoplanatic angle, θ_0 is not affected by the removal of aero-optical contamination. θ_0 is sensitive to turbulence deep into the path. Thus, for an A2G system the removal of the first two bins nearest to the aircraft does not have much impact on the θ_0 measurements. Generally, the HV57 and LEEDR models underestimate the measured isoplanatic angle. The measured and modeled Greenwood Frequencies are presented in (e) and (f). The removal of the aero-optical contamination significantly influences the results. With contamination, many of the measurements are around 200 Hz, but without contamination those same measurements fall to around 100 Hz. Several measurements are originally over 700 Hz, but without contamination, the magnitudes are significantly lower and more closely align with the HV57 model. The Tyler Frequency, presented in (g) and (h), is influenced similarly. The Tyler Frequency measurements are mostly halved due to the removal of the aero-optical contamination. Similarly, the Tyler Frequency measurements are more consistent with the HV57 model and LEEDR model. The Greenwood Frequency and Tyler Frequency are computed from the C_n^2 profile and wind profile. By removing the aero-optical contamination, the C_n^2 and wind profiles are reduced. Since the profiles containing the aero-optical contamination have high values in the first two

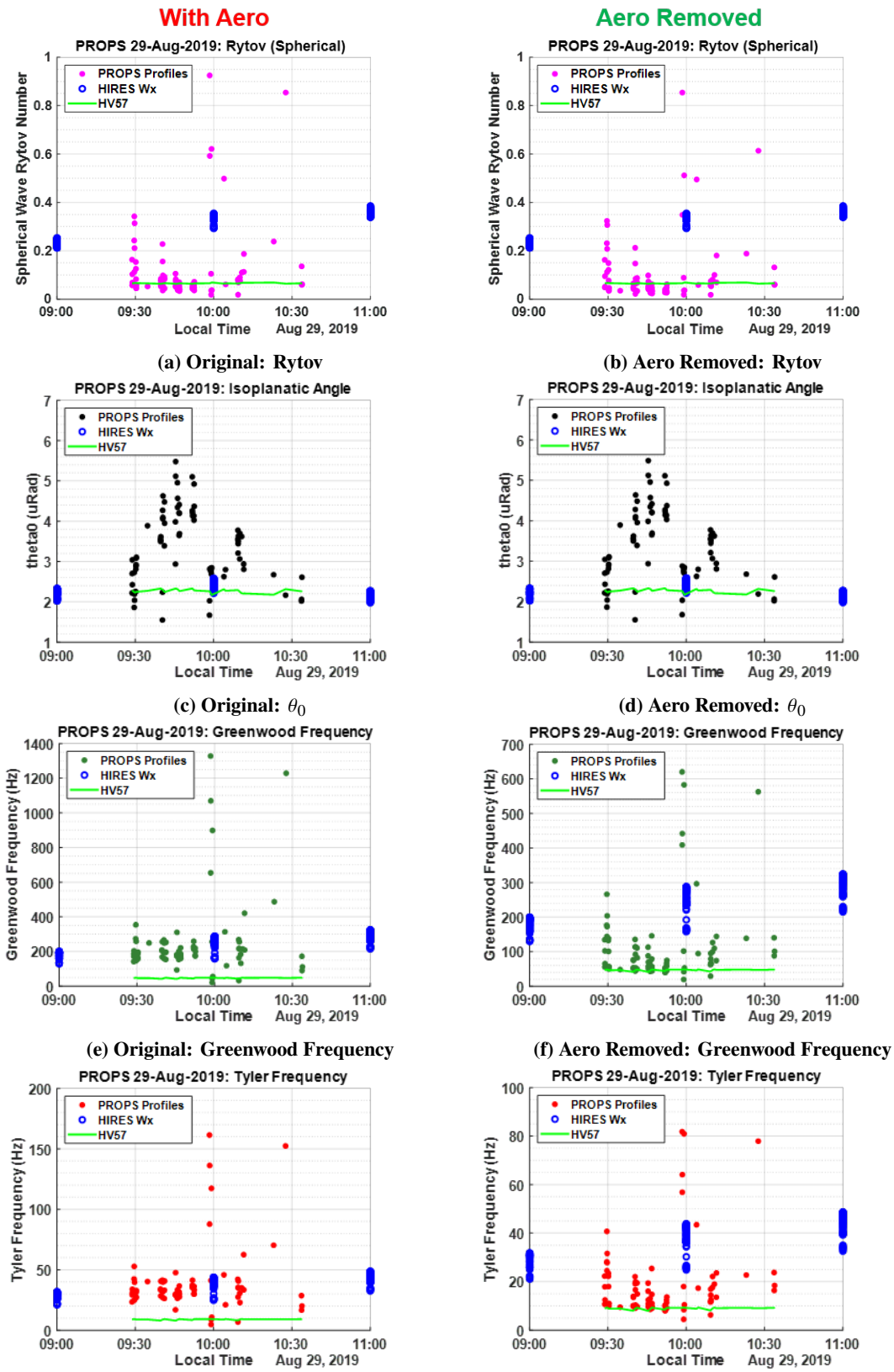

(a) Original: Rytov

(b) Aero Removed: Rytov

(c) Original: θ_0

(d) Aero Removed: θ_0

(e) Original: Greenwood Frequency

(f) Aero Removed: Greenwood Frequency

(g) Original: Tyler Frequency

(h) Aero Removed: Tyler Frequency

Fig. 15 System performance parameters with and without aero-optical contamination.

bins, the Greenwood Frequency and Tyler Frequency significantly decrease when those bins are removed.

These optical parameters can be extended to system performance parameters. Figure 16 compares system performance parameters for same A2G system – spherical coherence diameter r_0, open loop jitter, and open loop Strehl – between results with and without the aero-optical contamination. The top row contains results with aero-optical contamination. The bottom row contains results without contamination. Each of these performance measurements change significantly with the removal of aero-optical contamination. Beginning with coherence diameter, r_0, in plots (a) and (d), the removal of aero-optical contamination results in significantly larger values for many of the measurements, indicating atmospheric turbulence is less than originally measured. This result is expected since the bins removed have been shown to be significant turbulence enhancements. With contamination, r_0 is more consistent with the sparse LEEDR modeling than the HV57 model. The r_0 measurements with the aero-optical contamination removed are less clustered. Figure 16 (b) and (e) shows atmospheric open loop jitter which mostly decreases with the removal of aero-optical contamination. Originally, the measurements are clustered more around the LEEDR model, but with contamination removal the open loop jitter values, they become clustered closer to the HV57. Figure 16 (c) and (f) present open loop Strehl with and without tilt-removal (TR). For both, the measured open loop Strehl significantly increases when aero-optical contamination is removed. Many of the tilt-removed Strehl measurements (red points) are clustered around HV57 tilt-removed Strehl.

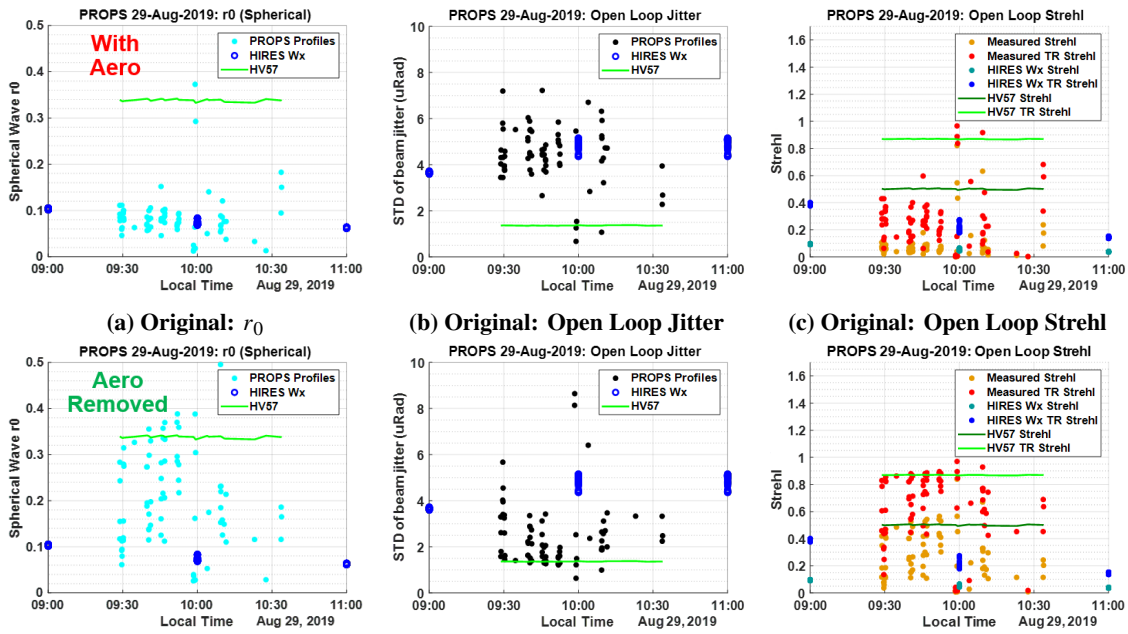

(a) Original: r_0 (b) Original: Open Loop Jitter (c) Original: Open Loop Strehl

(d) Aero Removed: r_0 (e) Aero Removed: Open Loop Jitter (f) Aero Removed: Open Loop Strehl

Fig. 16 System performance parameters with and without aero-optical contamination.

C. System Performance Modeling Comparison Between A2G and G2A

This section presents a comparison of system measurements and modeling between A2G and G2A engagements. All results in this section are free from aero-optical contamination, so some of the A2G plots are identical to A2G "Aero Removed" results presented in the previous section. For slant path engagements, the system performance and system capabilities will drastically differ between up-looking systems versus down-looking systems. Figure 17 compares A2G (left column) and G2A (right column) measurement parameters: spherical wave Rytov number, Isolplanatic Angle, Greenwood Frequency, and Tyler Frequency. Like before, each plot contains three sets of data: PROPS measurements, LEEDR weather cube models from HIRESW data, and HV57 model. Plots (a) and (b) confirm that Rytov weighting function is symmetric between each terminal. For a particular turbulence profile, Rytov number does not change between an A2G and G2A system. Plots (c) and (d) compare Isoplanatic Angle, θ_0, and illustrate the difference between terminals. The measured isoplantic angles from G2A are mostly much higher than from A2G, as expected. Since θ_0 is sensitive to turbulence out in the path, an A2G system observes smaller isoplantic angles than an up-looking G2A

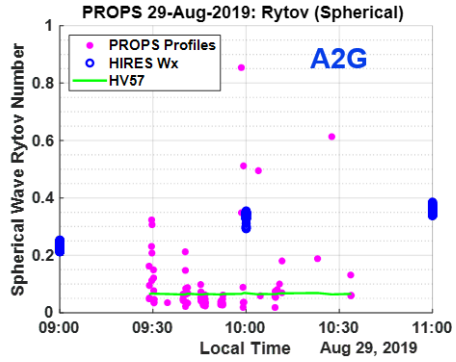

(a) A2G: Rytov

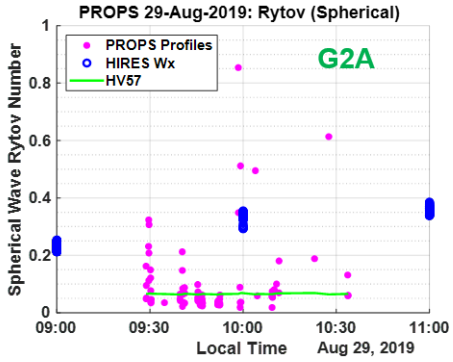

(b) G2A: Rytov

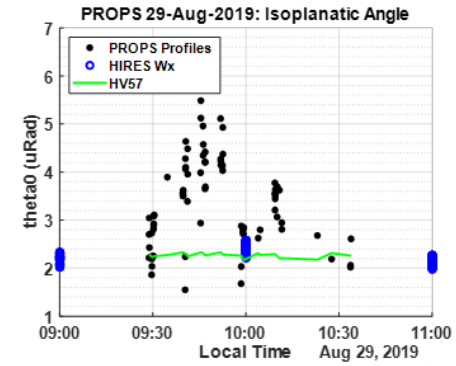

(c) A2G: θ_0

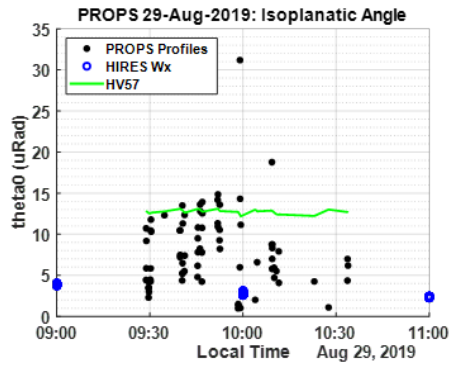

(d) G2A: θ_0

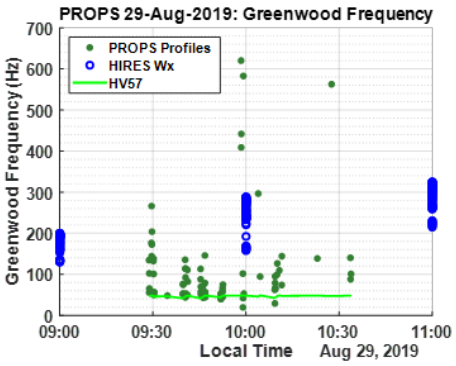

(e) A2G: Greenwood Frequency

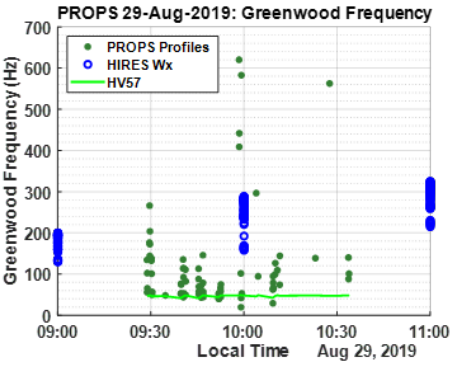

(f) G2A: Greenwood Frequency

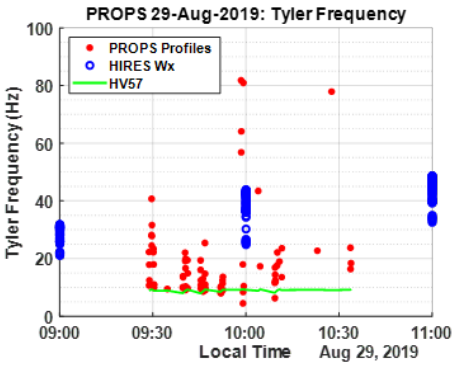

(g) A2G: Tyler Frequency

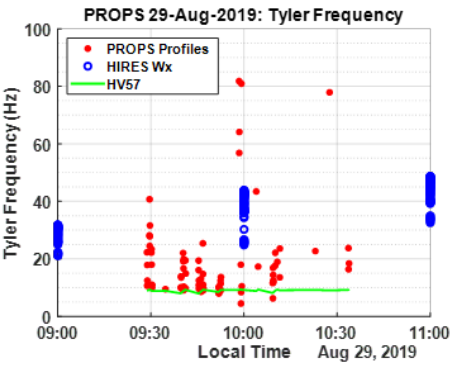

(h) G2A: Tyler Frequency

Fig. 17 Air-to-Ground (A2G) vs Ground-to-Air (G2A) system performance parameters without aero-optical contamination.

system. Plots (e) and (f) show the same Greenwood Frequency results from each terminal. This symmetry is expected since Greenwood Frequency is derived from C_n^2 and wind profiles. If the measurement is made from one terminal, the results are the same as from the other terminal because the C_n^2 and wind profiles reverse orientation, yielding the same data for calculation of Greenwood Frequency. For the same reason, plots (g) and (h) show the same Tyler Frequency results from each terminal. For Greenwood and Tyler Frequencies, the HV57 underpredicts while LEEDR overpredicts.

Furthermore, the optical parameters can be extended to other system performance metrics. The results are obtained using the same example system with a 30cm aperture operating at wavelength of 1μm. Figure 18 shows the system performance modeling parameters – spherical wave r_0, open loop jitter, and open loop Strehl – for a G2A engagement. It is apparent that the models are pessimistic, showing r_0 values that are generally lower than measurements. While the HV57 and LEEDR models forecast r_0 to be approximately 6cm, the PROPS measurements show r_0 values ranging from 5cm to 15cm. Thus, the modeled r_0 values are reasonable but pessimistic. The open loop jitter plot in the center of Figure 18, shows a similar performance trend. Open loop jitter is a function of r_0 and inversely proportional [17, 18]. The modeling forecasts a standard deviation of beam jitter to be 5-6 μrad. However, the measurement mostly reported open loop jitter under 5μrad. For context, the tracking PROPS terminal at the ground station described in Section II had two optical tracking systems (Acquistion Track System (ATS) and Fine Track System (FTS)). The instantaneous field-of-view (IFOV) of the ATS, which provides the WFOV, was set to 62.7μrad and the IFOV of the FTS, which provides the NFOV, was set to 1.65μrad. For a G2A system with similar IFOVs, the jitter created by uncompensated atmosphere shown in Figure 18 is a small fraction of a pixel in the ATS and 2-4 pixels in the FTS. In those terms, the HV57 and LEEDR models' forecast anticipates around 4 pixels of atmospheric jitter however the measurements indicated an observed 2-4 pixels throughout the data collection. Similarly, Figure 18 also shows the open loop Strehl ratio (right). The Strehl ratio and tilt-removed Strehl are also a function of r_0 [19]. This plot contains several key trends. First, for a G2A system, the strongest turbulence along the propagation path is near the aperture, and therefore the Strehl ratio is relatively small. Second, the HV57 model and LEEDR model are in agreement and indicate a Strehl of approximately 3% to 5%. The PROPS measurements show the Strehl varying from 2% to 16%. Third, by removing the tilt, the Strehl ratio significantly increases. The tilt-removed values are representative of having an ideal fast steering mirror (FSM) in the system that corrects for the tilt disturbances. The tilt-removed values, indicated in Figure 18 by a 'TR', are 10% to 15% for the models and 10% to 60% for the PROPS measurements. Lastly, as observed in previous plots, the HIRESW LEEDR model does not have the temporal resolution to capture trends occurring at the minute-by-minute scale. Overall, the models tend to be underrating the G2A system performance measurements.

In a similar way, the system performance can be modeled using the same system parameters and the same turbulence profiles, but with a reversed operation geometry. Figure 19 shows A2G engagement system performance modeling results. Here, the LEEDR models are highly pessimistic, mostly resulting in underrated performance relative to measurements. The r_0 of the LEEDR model range from 6cm to 10cm, while the HV57 model indicates a r_0 around 34cm. The PROPS r_0 measurements fluctuate significantly spanning the range of 2cm to 40cm. These fluctuations in the measurements translate to large fluctuations in the measured open loop jitter and open loop Strehl. The open loop jitter indicated the LEEDR are 4-5μrad, while the HV57 model shows 1.5μrad. The PROPS measurements fall in between the two models. For context, similar to the ground station, the tracking PROPS terminal at the air station also had two optical systems (ATS and FTS). The IFOV of the ATS, which provides the WFOV, was set to 43.1μrad and the IFOV of the FTS, which provides the NFOV, was set to 7.5μrad. For an A2G system with similar IFOVs, the jitter created by

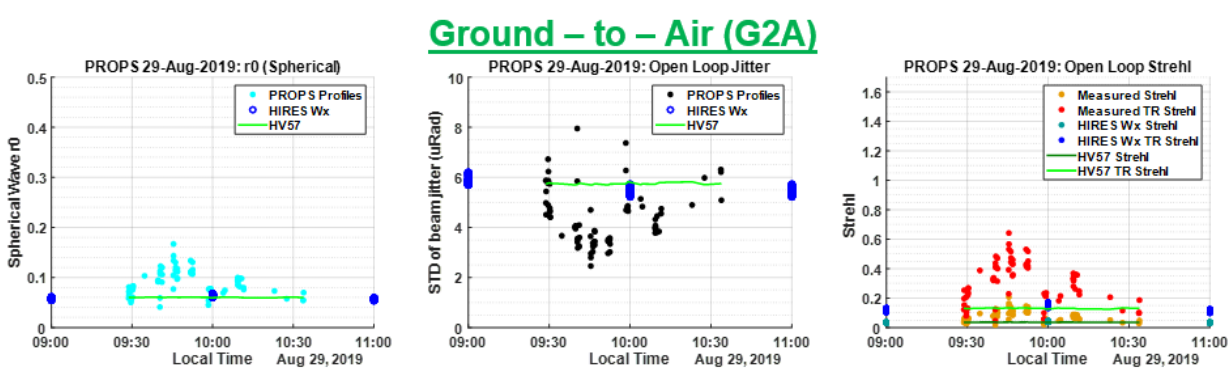

Fig. 18 Ground-to-Air (G2A) system performance.

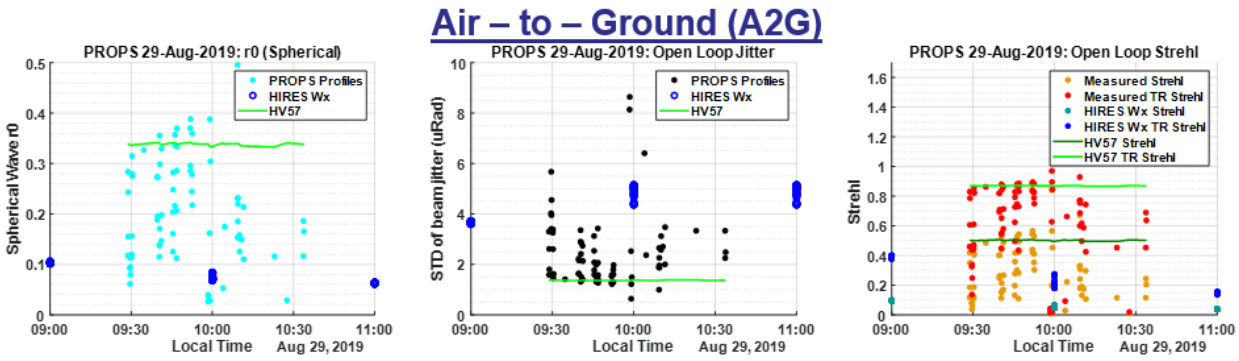

Fig. 19 Air-to-Ground (A2G) system performance.

the uncompensated atmosphere is a negligible fraction of a pixel in the ATS and about $\frac{1}{5}$ pixels in the FTS. The Strehl and tilt-removed Strehl ratios are significantly higher for the A2G as compared to the G2A system. Since the strong turbulence is away from the aperture, and the aero-contamination has been removed, the A2G provides more favorable atmospheric conditions for imaging and optical propagation. In Figure 19, the open loop Strehl plot (right) shows the HV57 model at 50% and LEEDR spanning 15% to 40%. The PROPS measurements vary from 2% to 60%. The tilt removed Strehl significantly improves the system performance. The tilt-removed HV57 model and many tilt-removed PROPS measurements show a 90% Strehl ratio. The conclusions and key findings are summarized in Section VI.

VI. Conclusion

The 2019 AAOL-BC flight experiments resulted in a vast amount of PROPS measurements. The 8km slant (2km altitude AGL) path C_n^2 measurements enable model validation and system performance analysis. For a direct comparison between models to measurements, the aero-optical contamination of the PROPS profiles was removed by eliminating the profile bins closest to the aircraft. Atmospheric PROPS measurements were compared to the standard HV57 model and an enhanced version of the HIRESW LEEDR weather cubes. The measurements confirmed an existing power law altitude scaling relationship between C_n^2 and altitude AGL near the surface. The analysis also shows occasional strong agreement in trends between modeling and measurements at higher altitudes. On the other hand, the analysis also revealed important deviation between modeling and measurements. Specifically, the strong deviations and discontinuities occur when the LEEDR model transitions from surface level modeling to the NWP calculations. These findings will lead to improvements in the LEEDR turbulence modeling. Analyzing system performance metrics such as open loop jitter and open loop Strehl shows that conditions are significantly different for A2G and G2A systems operating within the same turbulence conditions. The analysis also shows that HV57 and LEEDR agree with the PROPS and are both reasonable models for forecasting system performance conditions. For the experimental data presented, the HV57 model tends to be optimistic and LEEDR model tends to be pessimistic. The PROPS measurements and analysis presented will aid the development of improved turbulence modeling and forecasting.

Acknowledgments

We acknowledge and thank the numerous organization that have supported this research and field measurements. This work is sponsored by the Joint Technology Office, Grant number FA9550-13-1-0001 and Office of Naval Research, Grant number N00014-18-1-2112. We thank the University of Notre Dame Institute for Flow Physics and Control and the support staff that helped with planning and designing the system aircraft integration. Special thanks to Phil Rollins for coordinating the test activities with Northern Jet Management, the aircraft pilots, and GRR air traffic control. Thank you to the Facilities & Operations coordinators at Coopersville Area Public School, the athletic fields have proven to be an idea occlusion-free site for the ground station. The AFIT Center for Directed Energy group for aiding in the development and enhancement of LEEDR modeling and forecasting. Our advances are built on the outstanding work done with the LEEDR codes. Special thanks to WPAFB Base Ops, KFFO Air Field Management staff, WPAFB Security Forces, and AFRL/RYMM LADAR Technology branch for coordinating and facilitating the numerous long-range pre-flight ground tests and experiments necessary in support of this flight campaign.

References

[1] Kalensky, M., Jumper, E., Whiteley, M., Diskin, Y., Gordeyev, S., Drye, R., Archibald, A., and Grose, M., "Turbulence Profiling Using AAOL-BC," *AIAA Scitech 2020 Forum*, 2020, p. 0682.

[2] Gravley, L. E., "Comparison of climatological optical turbulence profiles to standard, statistical and numerical models using HELEEOS," Tech. rep., AIR FORCE INST OF TECH WRIGHT-PATTERSON AFB OH SCHOOL OF ENGINEERING AND . . . , 2006.

[3] Andrews, L. C., Phillips, R. L., Wayne, D., Leclerc, T., Sauer, P., Crabbs, R., and Kiriazes, J., "Near-ground vertical profile of refractive-index fluctuations," *Atmospheric Propagation VI*, Vol. 7324, International Society for Optics and Photonics, 2009, p. 732402.

[4] Andrews, L. C., and Phillips, R. L., "Laser beam propagation through random media," SPIE, 2005.

[5] Hardy, J. W., *Adaptive optics for astronomical telescopes*, Vol. 16, Oxford University Press on Demand, 1998.

[6] Bufton, J. L., "Comparison of vertical profile turbulence structure with stellar observations," *Applied optics*, Vol. 12, No. 8, 1973, pp. 1785–1793.

[7] Fiorino, S. T., Bartell, R. J., Krizo, M. J., Caylor, G. L., Moore, K. P., Harris, T. R., and Cusumano, S. J., "A first principles atmospheric propagation & characterization tool: the laser environmental effects definition and reference (LEEDR)," *Atmospheric Propagation of Electromagnetic Waves II*, Vol. 6878, International Society for Optics and Photonics, 2008, p. 68780B.

[8] Center, E. M., "The GFS atmospheric model," *National Centers for Environmental Prediction Office Note*, Vol. 442, 2003, p. 14.

[9] Diskin, Y., Whiteley, M., Magee, E., Schmidt, J., Wauligman, B., and Grose, M., "Surface Level Turbulence Modeling using Meteorological Observations," *Annual DE Science & Technology Symposium*, Directed Energy Professional Society, Destin, Florida, 2019.

[10] Diskin, Y., Grose, M., Magee, E., and Whiteley, M., "Enhanced Surface Level Turbulence Modeling and Forecasting," *Annual DE Science & Technology Symposium*, Directed Energy Professional Society, West Point, New York, 2020.

[11] Whiteley, M. R., "Rytov parameter estimation by use of differential-tilt measurements," *Propagation and Imaging through the Atmosphere IV*, Vol. 4125, edited by M. C. Roggemann, International Society for Optics and Photonics, 2000, pp. 7–20.

[12] Whiteley, M. R., Washburn, D. C., and Wright, L. A., "Differential-tilt technique for saturation-resistant profiling of atmospheric turbulence," *Adaptive Optics Systems and Technology II*, Vol. 4494, International Society for Optics and Photonics, 2002, pp. 221–232.

[13] Jumper, E. J., and Fitzgerald, E. J., "Recent advances in aero-optics," *Progress in Aerospace Sciences*, Vol. 37, No. 3, 2001, pp. 299–339.

[14] De Lucca, N., Gordeyev, S., and Jumper, E., "The airborne aero-optics laboratory, recent data," *Acquisition, Tracking, Pointing, and Laser Systems Technologies XXVI*, Vol. 8395, International Society for Optics and Photonics, 2012, p. 839508.

[15] Jumper, E. J., Gordeyev, S., Cavalieri, D., Rollins, P., Whiteley, M., and Krizo, M., "Airborne aero-optics laboratory-transonic (aaol-t)," *53rd AIAA Aerospace Sciences Meeting*, 2015, p. 0675.

[16] Jumper, E. J., Zenk, M. A., Gordeyev, S. V., Cavalieri, D. A., and Whitely, M., "Airborne aero-optics laboratory," *Optical Engineering*, Vol. 52, No. 7, 2013, p. 071408.

[17] Shellan, J. B., "Statistical properties of the Strehl ratio as a function of pupil diameter and level of adaptive optics correction following atmospheric propagation," *JOSA A*, Vol. 21, No. 8, 2004, pp. 1445–1451.

[18] Widiker, J. J., and Magee, E. P., "Open-loop simulations of atmospheric turbulence using the AdAPS interface," *Advanced Wavefront Control: Methods, Devices, and Applications III*, Vol. 5894, International Society for Optics and Photonics, 2005, p. 589404.

[19] Valley, G. C., "Long-and short-term Strehl ratios for turbulence with finite inner and outer scales," *Applied optics*, Vol. 18, No. 7, 1979, pp. 984–987.